
ENERGY NETWORKS FOR STATE ESTIMATION WITH RANDOM SENSORS USING SPARSE LABELS

A PREPRINT

Yash Kumar

Department of Mechanical Engineering
Delhi Technological University
Shahbad Daulatpur, Main Bawana Road, Delhi-110042, India
yashk8481@gmail.com

Souvik Chakraborty

Department of Applied Mechanics
Indian Institute of Technology Delhi
Hauz Khas - 110042, New Delhi, India
souvik@am.iitd.ac.in

March 15, 2022

ABSTRACT

State estimation is required whenever we deal with high-dimensional dynamical systems, as the complete measurement is often unavailable. It is key to gaining insight, performing control or optimizing design tasks. Most deep learning-based approaches require high-resolution labels and work with fixed sensor locations, thus being restrictive in their scope. Also, doing Proper orthogonal decomposition (POD) on sparse data is nontrivial. To tackle these problems, we propose a technique with an implicit optimization layer and a physics-based loss function that can learn from sparse labels. It works by minimizing the energy of the neural network prediction, enabling it to work with a varying number of sensors at different locations. Based on this technique we present two models for discrete and continuous prediction in space. We demonstrate the performance using two high-dimensional fluid problems of Burgers' equation and Flow Past Cylinder for discrete model and using Allen-Cahn equation and Convection-diffusion equations for continuous model. We show the models are also robust to noise in measurements.

Keywords State estimation · Differentiable implicit layers · Dynamical systems

1 Introduction

State estimation is the ability to recover flow based on a few measurements. It is an inverse problem and arises in many engineering applications such as remote sensing, medical imaging, ocean dynamics, reservoir modeling, and blood flow modeling. Uses of fluid estimation include flow control [1, 2], cardiac blood flow modeling [3, 4, 5], ship wake identification [6], climate prediction [7], optimizing machine design for low-drag vehicles, efficient turbo-machines, etc. Few challenges faced in the processes are limited sensors, sparse label data, moving sensors, ill-posed problems, noisy measurements, etc. This work focuses on learning from moving sparse label data and sensor measurements with a deep learning-based model using an implicit optimization layer for network training. Sparse fluid is encountered in various situations. One reason is that storing high-resolution data generated during direct numerical simulation is challenging due to limited storage space. It makes analysis, sharing, and visualization difficult. Another important reason is that real data is hard to measure on a full scale, like cardiovascular blood flow data obtained from flow magnetic resonance imaging (MRI) [8, 9, 10].

For high dimensional state estimation problems like fluids, popular approaches include library-based approaches observer dynamical system stochastic approaches. Library-based methods use offline data, and the library consists of generic modes such as Fourier, wavelet, discrete cosine transform basis, or data specific Proper orthogonal decomposition (POD) or Dynamic mode decomposition (DMD) modes, or training data. Library-based approaches using sparse representation assume state can be expressed as the combination of library elements. In an observer dynamical system, we assume the system's dynamics to produce a full state and update it based on new measurements to reduce estimation error forming a closed feedback loop. The estimate is maintained by Kalman filtering [11, 12, 13]. Tu et al. [14] applied

dynamic mode decomposition [15, 16] as a reduced-order model to Kalman smoother estimate to identify coherent structures. Buffoni et al. [17] used a nonlinear observer-based on Galerkin projection of Navier-Stokes equation to estimate POD coefficients. Stochastic estimation was proposed by Adrian [18] for a turbulence study where the conditional mean was approximated using a power series. Extension to this method [19, 20, 21] can be found in the literature. Bonnet et al. [22] extended stochastic approach to estimate POD coefficients. A linear mapping between sensors and coefficients was assumed. These approaches allow more flexibility in sensor placements and have been applied for flow control over airfoil [23] and analyzing isotropic turbulence [24, 25].

We consider a problem with sparse label data whose position may vary with time, for which POD can not be performed. Thus it restricts us from using traditional POD-based approaches. Other deep learning-based approaches like [26, 27, 28] give accurate predictions with fewer sensors but require high-resolution labels for training. Gao et al. [29] uses physics-based loss for super-resolution using spare data and thus assumes a fixed number of sensors and their positions. In this work, we propose an Energy network for state estimation with random sensors (ENSERS), a technique to learn a model from spare training labels capable of predicting full states given a varied number of sensors at random locations. We present two models trained using this technique. The first one produces discrete high-dimensional predictions in space. Second, produce continuous prediction utilizing the information of coordinates. We demonstrate the results corresponding to four high complexity problems: 2-dimensional (2D) coupled Burgers' equation, transient flow, Allen-Cahn equation, and Convection-diffusion equation.

The remainder of the paper is organized as follows. In Section 2, details on the problem statement is provided. Details on the proposed approach are provided in Section 3.1. Section 3 and 4 give details on discrete and continuous formulation with two numerical examples in each to illustrate the performance of the proposed approach. Finally, Section 5 provides the concluding remarks.

2 Problem statement

Consider a dynamical system obtained by partial discretization of the d -dimensional governing differential equations:

$$J_t(x, t) = F(x, J(x, t)), \quad J^n = J(x, t_n), \quad x \in \Omega \quad (1)$$

The simulation time domain is discretized by L steps and the space domain is discretized by ω segments resulting in

$$Z = \{J_m^l \in \mathbb{R}^\omega \mid l = 0, \dots, L-1, m = 0, \dots, M-1\} \quad (2)$$

where $Z \in \mathbb{R}^{L \times M \times \omega}$, l is time step index, M = number of system's state variables. e.g. $m = 0$ represents x-velocity and $m = 1$ represents y-velocity in § 3.2 of 2D coupled Burgers' equation. We consider sensor location and data location, represented by integers in discrete domain respectively as

$$S = \{\lambda_m^l \in \mathbb{Z}^p \cap [0, \omega - 1]^p \mid l = 0, \dots, L-1, m = 0, \dots, M-1\} \quad (3)$$

$$T = \{\pi_m^l \in \mathbb{Z}^h \cap [0, \omega - 1]^h \mid l = 0, \dots, L-1, m = 0, \dots, M-1\} \quad (4)$$

where p = number of sensors, h = number of data nodes, $S \in \mathbb{Z}^{L \times M \times p} \cap [0, \omega - 1]^{L \times M \times p}$, $T \in \mathbb{Z}^{L \times M \times h} \cap [0, \omega - 1]^{L \times M \times h}$. The corresponding sensor values and data values are

$$X = \{\sigma_m^l \in \mathbb{R}^p \mid l = 0, \dots, L-1, m = 0, \dots, M-1\} \quad (5)$$

$$\Phi = \{\psi_m^l \in \mathbb{R}^h \mid l = 0, \dots, L-1, m = 0, \dots, M-1\} \quad (6)$$

$$\sigma_m^l = \Lambda_m^l J_m^l \quad (7)$$

$$\psi_m^l = \Pi_m^l J_m^l \quad (8)$$

where $X \in \mathbb{R}^{L \times M \times p}$, $\Phi \in \mathbb{R}^{L \times M \times h}$. $\Lambda_m^l \in \mathbb{R}^{p \times \omega}$ and $\Pi_m^l \in \mathbb{R}^{h \times \omega}$ are measurement matrices composed of one-hot row vectors. Λ_m^l and Π_m^l are defined as

$$\Lambda_{mij}^l = \begin{cases} 1 & \text{if } \lambda_{mi}^l = j \\ 0 & \text{otherwise} \end{cases} \quad (9)$$

$$\Pi_{mij}^l = \begin{cases} 1 & \text{if } \pi_{mi}^l = j \\ 0 & \text{otherwise} \end{cases} \quad (10)$$

Note that integer sensor locations λ_m^l are selected randomly and are kept fixed during training. Similarly, a different set of sensor locations S is selected for testing the network. In this work, we aim to use sensor data from a set of γ system states and produce γ high dimensional states. Thus we divided the sensor values and data into chunks, each with γ states.

$$\chi^k = \{\sigma_m^{k*z+i} \in \mathbb{R}^p \mid i = 0, \dots, \gamma-1, m = 0, \dots, M-1\} \quad (11)$$

$$\phi^k = \{\psi_m^{k*z+i} \in \mathbb{R}^h \mid i = 0, \dots, \gamma-1, m = 0, \dots, M-1\} \quad (12)$$

where $\chi^k \in \mathbb{R}^{\gamma \times M \times p}$ are sensor values for γ time steps, $\phi^k \in \mathbb{R}^{\gamma \times M \times h}$ are data values for γ time steps, $k = 0, \dots, N-1$, N is number of train samples, z is time steps between first state σ_m^{k*z} of each tensor χ^k .

3 Discrete space models

3.1 Proposed approach

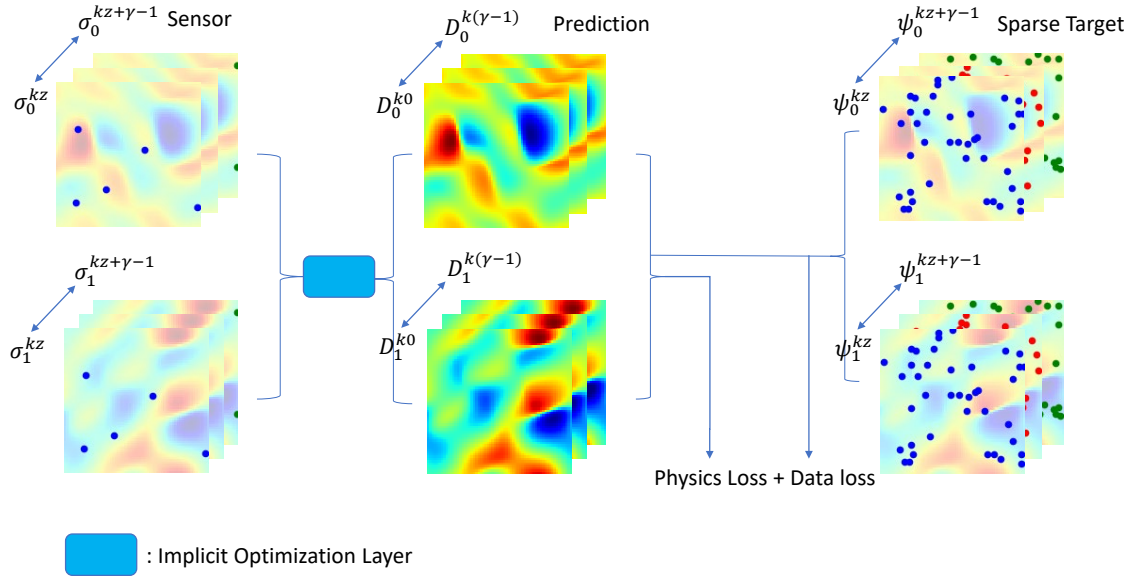


Figure 1: Network architecture of proposed Enzers model.

In this section, we propose a novel deep learning-based framework for state estimation. Prediction of γ high dimensional states is done via feed-forward neural network (FNN) Γ using optimized reduced state vector $\xi^k \in \mathbb{R}^\omega$:

$$\Gamma(\xi^k) = D^k = \{D_m^{ki} \in \mathbb{R}^\omega \mid i = 0, \dots, \gamma-1, m = 0, \dots, M-1\} \quad (13)$$

where $D^k \in \mathbb{R}^{\gamma \times M \times \omega}$ is a third-order tensor of predicted states. The output vector of FNN has a dimension of $\gamma * M * \omega$ which is reshaped into a tensor of shape $\gamma \times M \times \omega$. The reduced state is obtained by solving the following minimization problem using sensor data χ^k and predicted states by the neural network.

$$\xi^k = \arg \min_{\xi^k} \|\text{vec}(\chi^k - \rho(\tilde{\xi}^k))\|_2^2 \quad (14a)$$

$$\rho(\tilde{\xi}^k) = \{\tilde{Q}_m^{ki} \in \mathbb{R}^p \mid i = 0, \dots, \gamma - 1, m = 0, \dots, M - 1\} \quad (14b)$$

$$\tilde{Q}_m^{ki} = \Lambda_m^{kz+i} \tilde{D}_m^{ki} \quad (14c)$$

$$\Gamma(\tilde{\xi}^k) = \{\tilde{D}_m^{ki} \in \mathbb{R}^\omega \mid i = 0, \dots, \gamma - 1, m = 0, \dots, M - 1\} \quad (14d)$$

where $\tilde{Q}_m^{ki} \in \mathbb{R}^p$ are values of predicted states at sensor locations λ_m^{kz+i} , $\Lambda_m^{kz+i} \in \mathbb{R}^{p \times \omega}$ is measurement matrix. Note that in practice $\tilde{\xi}^k$ is obtained by a few steps of gradient descent instead of global minimization. This inner optimization loop is implemented using the library ‘higher’ [30] in PyTorch. Also, dimension ζ of the reduced state vector is quite small (e.g. 8 in first experiment § 3.2) therefore the time required for gradient descent steps is negligible. The network Γ is trained by minimizing data loss and physics-based loss $P(\chi^k)$ across training samples N .

$$\theta^* = \arg \min_{\theta} \sum_{k=0}^{N-1} \|\text{vec}(\phi^k - \Upsilon(\chi^k))\|_2^2 + P(\chi^k) \quad (15a)$$

$$\Upsilon(\chi^k) = \{Y_m^{ki} \in \mathbb{R}^h \mid i = 0, \dots, \gamma - 1, m = 0, \dots, M - 1\} \quad (15b)$$

$$Y_m^{ki} = \Pi_m^{kz+i} D_m^{ki} \quad (15c)$$

where $D_m^{ki} \in \mathbb{R}^\omega$ are predicted states by network Γ from Eq. (13), $Y_m^{ki} \in \mathbb{R}^h$ are values of predicted states at data locations π_m^{kz+i} , $\Upsilon(\chi^k)$ are predicted states composed of γ time steps. Fig. 1 shows the network architecture during training. Equations (13) and (14) together forms the implicit optimization layer shown in the Fig. 1. Training and testing procedure is shown in Algorithm 1 and 2 respectively. Note that for demonstration purpose, in all Algorithms a batch size of 1 is considered but in practice batch size is selected based on problem as mentioned in each experiment section. Also we use Huber loss function during testing as it is more robust to noise than mean squared error (MSE) loss function.

Methods based on implicit optimization layers come under the category of Optimization-based Modeling architectures [31] and are well-studied for generic classification, and structured prediction tasks [32, 33, 34, 35]. The most common way of training such models is through Unrolled Differentiation [36, 37, 38, 33]. It is done by introducing an optimization procedure such as gradient descent into the inference procedure. Other ways of training include Implicit argmin differentiation using implicit function theorem but need argmin operations to be convex. This method can be found in works of [39, 40]. In this work, we use Unrolled Differentiation technique for training.

3.1.1 Physics-based loss function

The physics-based loss function is used in the approach because of spare training labels. Training any network with just spare labels will produce garbage values on nodes without labels. Physics-based loss functions have been used to train neural networks for solving PDEs. A popular class of methods is PINNs [41]. The basic idea here is to place a neural network prior to the state variable and then estimate the neural network parameters by using a physics-informed loss function. Several improvements to the originally proposed PINN can also be found in the literature. For example, Zhu et al. [42] developed convolutional PINN for time-independent systems. Geneva and Zabarabas [43] used physics constrained auto-regressive model for surrogate modeling of dynamical systems. We use Runge-Kutta methods with q stages for defining loss between γ state predictions. Let

$$V^n = D^{k0} \quad (16a)$$

$$V^{n+c_i} = D^{ki}, \quad i = 1, \dots, q \quad (16b)$$

$$V^{n+1} = D^{k(\gamma-1)} \quad (16c)$$

where D^{ki} are network prediction. General form of Runge-Kutta methods with q stages applied to Eq. (1):

$$V^{n+c_i} = V^n - \Delta t \sum_{j=1}^q a_{ij} F(V^{n+c_j}), \quad i = 1, \dots, q \quad (17a)$$

Algorithm 1: Training ENSERS

```

1: Inputs:  $Z, S, T$ . {Eq. (2), Eq. (3), Eq. (4)}
2: Set Hyper-parameters:  $\eta_o$ : outer learning rate,  $\eta_{i0}$ : inner learning rate at epoch=0,  $\hat{\eta}_i$ : inner learning rate rate,  $\beta$ :
   batch size,  $I_o$ : outer iterations,  $I_i$ : inner iterations,  $\hat{\zeta}$ : physics penalty rate,  $\zeta_0$ : physics penalty at epoch=0,  $N$ :
   number of train samples,  $z, \gamma$ .
3: Calculate data-set:  $\chi, \phi, \Lambda, \Pi$ 
4: Initialize: Neural network model:  $\Gamma(\cdot; \theta)$ 
5: for  $\iota_o = 0$  to  $I_o - 1$  do {Outer optimization Loop}
6:    $\eta_i = \eta_{i0} + \iota_o \hat{\eta}_i$  {Schedule inner learning rate}
7:    $\zeta = \zeta_0 + \iota_o \hat{\zeta}$  {Schedule physics penalty}
8:   for  $k = 0$  to  $N - 1$  do
9:     Initialize:  $\tilde{\xi}^k$ 
10:    for  $\iota_i = 0$  to  $I_i - 1$  do {Inner optimization Loop}
11:       $\tilde{D}^k = \Gamma(\tilde{\xi}^k)$  {Eq. (14d)}
12:       $\tilde{Q}^k \leftarrow \text{DrawValuesAtSensorLocations}(\tilde{D}^k)$  {Eq. (14c)}
13:       $\mathcal{L} = \text{MSE}(\chi^k, \tilde{Q}^k)$ 
14:       $\frac{\partial \mathcal{L}}{\partial \tilde{\xi}^k} \leftarrow \text{Backprop}(\mathcal{L})$ 
15:       $\tilde{\xi}^k = \tilde{\xi}^k - \eta_i \frac{\partial \mathcal{L}}{\partial \tilde{\xi}^k}$ 
16:    end for
17:     $\xi^k = \tilde{\xi}^k$ 
18:     $D^k = \Gamma(\xi^k)$  {Eq. (13)}
19:     $Y^k \leftarrow \text{DrawValuesAtDataLocations}(D^k)$  {Eq. (15c)}
20:     $\mathcal{L} = \text{MSE}(\phi^k, Y^k) + \zeta P(D^k)$  {Calculate loss}
21:     $\frac{\partial \mathcal{L}}{\partial \theta} \leftarrow \text{Backprop}(\mathcal{L})$ 
22:     $\theta \leftarrow \theta - \eta_o \frac{\partial \mathcal{L}}{\partial \theta}$  {Update weights}
23:  end for
24: end for
25: Output: Trained network  $\Gamma(\cdot; \theta^*)$ .

```

Algorithm 2: Testing ENSERS

```

1: Inputs: Trained network  $\Gamma(\cdot; \theta^*)$ ,  $S$ . {Eq. (3)}
2: Set Hyper-parameters:  $\eta_i$ : inner learning rate,  $I_i$ : inner iterations,  $\hat{N}$ : number of test samples,  $z, \gamma$ .
3: Calculate data-set:  $\chi, \Lambda$ 
4: for  $k = 0$  to  $\hat{N} - 1$  do
5:   Initialize:  $\tilde{\xi}^k$ 
6:   for  $\iota_i = 0$  to  $I_i - 1$  do {Inner optimization Loop}
7:      $\tilde{D}^k = \Gamma(\tilde{\xi}^k)$  {Eq. (14d)}
8:      $\tilde{Q}^k \leftarrow \text{DrawValuesAtSensorLocations}(\tilde{D}^k)$  {Eq. (14c)}
9:      $\mathcal{L} = \text{MSE}(\chi^k, \tilde{Q}^k)$ 
10:     $\frac{\partial \mathcal{L}}{\partial \tilde{\xi}^k} \leftarrow \text{Backprop}(\mathcal{L})$ 
11:     $\tilde{\xi}^k = \tilde{\xi}^k - \eta_i \frac{\partial \mathcal{L}}{\partial \tilde{\xi}^k}$ 
12:  end for
13:   $\xi^k = \tilde{\xi}^k$ 
14:   $D^k = \Gamma(\xi^k)$  {Eq. (13)}
15: end for
16: Output: Predicted states  $\{D_m^{ki} \mid k = 0, \dots, N - 1, i = 0, \dots, \gamma - 1, m = 0, \dots, M - 1\}$ .

```

$$V^{n+1} = V^n - \Delta t \sum_{j=1}^q b_j F(V^{n+c_j}) \quad (17b)$$

We use the Implicit Runge-Kutta methods with q stages and thus parameters $\{a_{ij}, b_j, c_j\}$ are chosen accordingly. Now, shifting second term on right hand side (RHS) in Eq. (17) to left hand side (LHS) and replacing exact operator F with numerical gradient based operator \hat{F}

$$\hat{W}_i = V^{n+c_i} + \Delta t \sum_{j=1}^q a_{ij} \hat{F}(V^{n+c_j}), \quad i = 1, \dots, q \quad (18a)$$

$$W_{q+1}^{\hat{}} = V^{n+1} + \Delta t \sum_{j=1}^q b_j \hat{F}(V^{n+c_j}) \quad (18b)$$

$$P(\chi^k) = \sum_{i=1}^{q+1} \|\text{vec}(\hat{W}_i - V^n)\|_2^2 \quad (18c)$$

where \hat{W}_i are different estimates of V^n , $P(\chi^k)$ is the physics based loss function. For calculating loss the spatial gradients are approximated using Sobel filter 2D convolutions [44]. See § A for additional details. Note that physics-based loss function is only used during training of network.

In next section, we present two examples to show model proposed is able to learn from sparse moving data labels. We illustrate the performance of the proposed approach with plots of prediction. We show that model is robust against noisy sensor measurements by showing error corresponding to various noise level. Error used as a quantitative metric in plots is defined as

$$\epsilon^k = \frac{\|D_m^{k\gamma^*} - J_m^{k*z+\gamma^*}\|_2}{\|J_m^{k*z+\gamma^*}\|_2} \quad k = 0, \dots, \hat{N} \quad (19)$$

where $\epsilon^k \in \mathbb{R}$ represents the error, \hat{N} number of test samples, $J_m^{k*z+\gamma^*} \in \mathbb{R}^\omega$ are the true state and $D_m^{k\gamma^*} \in \mathbb{R}^\omega$ are the predicted state using the proposed approach. $\|\cdot\|_2$ represents the L2 norm.

3.2 Experiment: 2D coupled Burgers' equation

As the first example, we consider the the 2D coupled Burgers' system. It has the same convective and diffusion form as the in-compressible Navier-Stokes equations. It is an important model for understanding of various physical flows and problems, such as hydrodynamic turbulence, shock wave theory, wave processes in thermo-elastic medium, vorticity transport, dispersion in porous medium. The governing equations for Burgers' equation takes the following form:

$$\mathbf{u}_t + \mathbf{u} \cdot \nabla \mathbf{u} - \nu \Delta \mathbf{u} = 0, \quad (20)$$

with periodic boundary condition

$$\begin{aligned} \mathbf{u}(x=0, y, t) &= \mathbf{u}(x=L, y, t), \\ \mathbf{u}(x, y=0, t) &= \mathbf{u}(x, y=L, t). \end{aligned} \quad (21)$$

Eq. (20) can be written in expanded form as

$$\begin{aligned} \frac{\partial u}{\partial t} + u \frac{\partial u}{\partial x} + v \frac{\partial u}{\partial y} - \nu \left(\frac{\partial^2 u}{\partial x^2} + \frac{\partial^2 u}{\partial y^2} \right) &= 0 \\ \frac{\partial v}{\partial t} + u \frac{\partial v}{\partial x} + v \frac{\partial v}{\partial y} - \nu \left(\frac{\partial^2 v}{\partial x^2} + \frac{\partial^2 v}{\partial y^2} \right) &= 0, \end{aligned} \quad (22)$$

where ν is viscosity, u and v are the x and y components of velocity. We consider $\{x, y\} \in [0, 1]$. The initial condition is defined using truncated Fourier series with random coefficients:

$$\mathbf{u}(x, y, t=0) = \frac{2\mathbf{w}(x, y)}{\max_{\{x, y\}} |\mathbf{w}(x, y)|} + \mathbf{c}, \quad (23)$$

where

$$w(x, y) = \sum_{i=-L}^L \sum_{j=-L}^L a_{ij} \sin(2\pi(ix + jy)) + b_{ij} \cos(2\pi(ix + jy)), \quad (24)$$

where $a_{ij}, b_{ij} \sim N(0, \mathbf{I}_2)$, $L = 4$ and $c \sim \mathcal{U}(-1, 1) \in \mathbb{R}^2$.

3.2.1 Data-set and Model Parameters

We use FeNICS [45] computing platform to solve the partial differential equations (22) for generating data-set. We discretize the spatial domain with 64×64 grid and use a time-step of 0.005. Parameters related to data-set considered are displayed in Table 1. We use noisy measurements to test the approach. Noise level is measured in signal to noise ratio (SNRdB) in decibels(dB) and is represented by SNR_{dB} . Signal after adding noise r is formulated as:

$$r = s + \left(\frac{P}{2 * 10^{\frac{SNR_{dB}}{10}}} \right)^{0.5} * \mathcal{N} \quad (25a)$$

$$P = \frac{\sum s^2}{n} \quad (25b)$$

where, s is noise-free signal, \mathcal{N} is random variable with standard normal distribution. Plots depicting different noise levels used for testing is shown in Fig. 2.

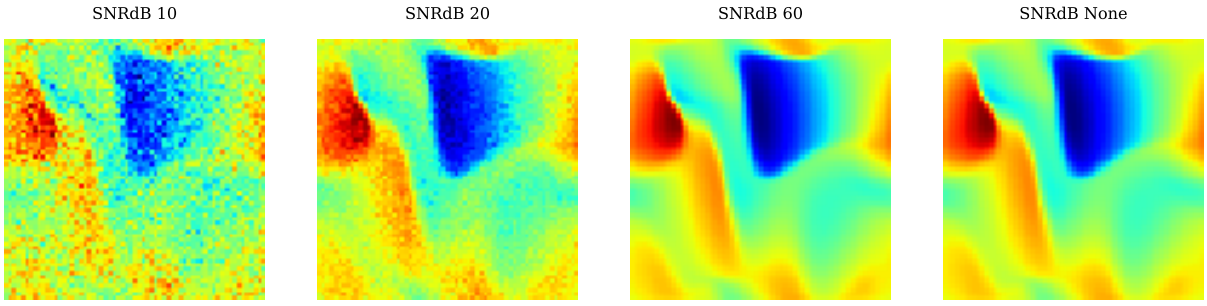


Figure 2: Plots of 2D Burgers velocity for visualizing different noise levels. SNRdB represents signal to noise ratio in decibels.

Table 1: Data-set parameters for 2D Burgers problem.

γ	M	L	z	ω	domain
5	2	50	2	3969	63×63

Table 2: Network architecture of proposed Enzers for 2D coupled Burgers' problem.

Layer	Input	Output	Activation
FC	8	64	Softplus
FC	64	64	Softplus
FC	64	$\omega * M * \gamma$	linear

Table 3: Training hyper parameters of Enzers for 2D Burgers problem.

η_o	η_{i0}	$\hat{\eta}_i$	β	I_o	I_i	ζ_0	$\hat{\zeta}$	p	h	N	ζ
0.0002	0.1	0.006	11	2001	4	0.005	0.0001	32	800	22	8

Table 4: Testing hyper-parameters of Enzers for 2D Burgers problem. η_i : inner learning rate, I_i : inner iterations

η_i	I_i	p	\hat{N}
5	100	[4, 16]	12

FNN used in the model is a shallow network with three fully connected (FC) layers. We use Softplus [46] activation function which has smooth first derivatives. Thus it helps avoid discontinuities because unrolling the inference procedure involves computing $\nabla_{\theta} \nabla_{\xi} (\mathcal{L})$. Network architecture is displayed in Table 2. We use 800 data nodes for training from each system variable data which is 20% of high-resolution data. Training hyper-parameters and training data are summarized in table 3. For testing, we use sensor locations different from the ones used during training.

3.2.2 Results and Discussions

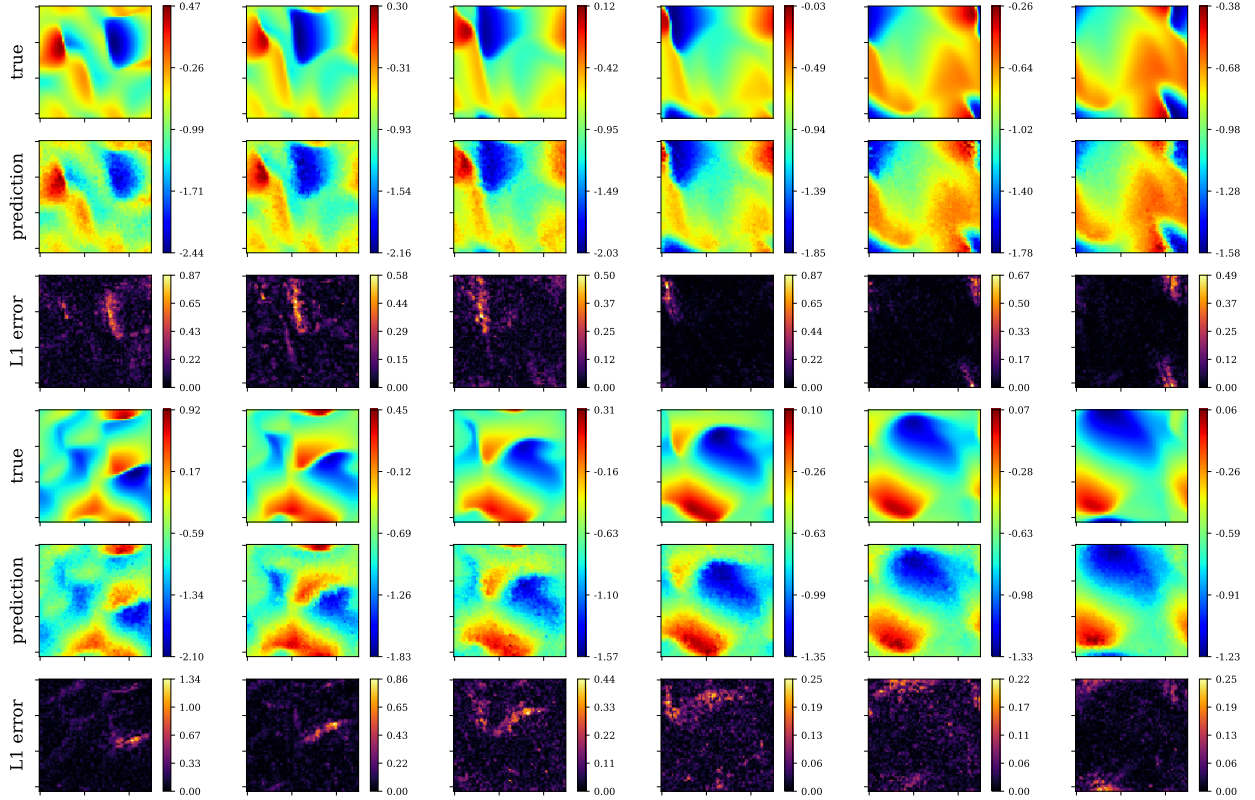


Figure 3: Ensens predictions of a 2D coupled Burgers' test case. (Top to bottom) x-velocity FEM target solution, x-velocity Ensens prediction, x-velocity L1error, y-velocity FEM target solution, y-velocity Ensens prediction and y-velocity L1error.

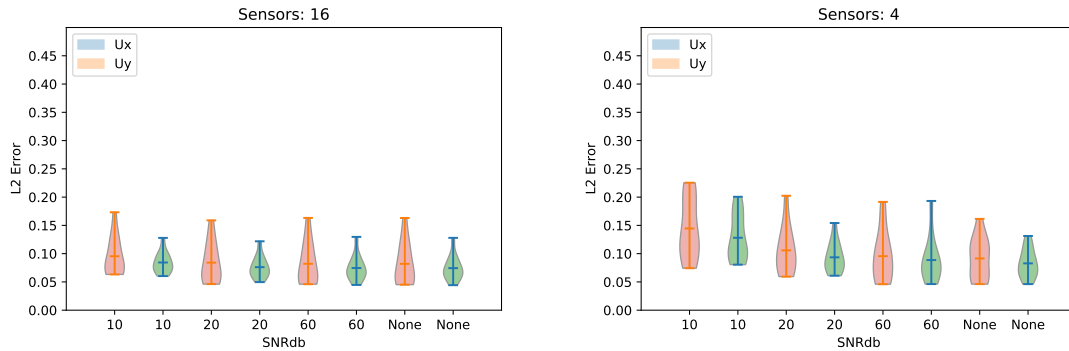


Figure 4: Violin plot representing error ε distribution in prediction vector of x and y velocity for different noise levels in sensor measurements for 2D coupled Burgers' test case.

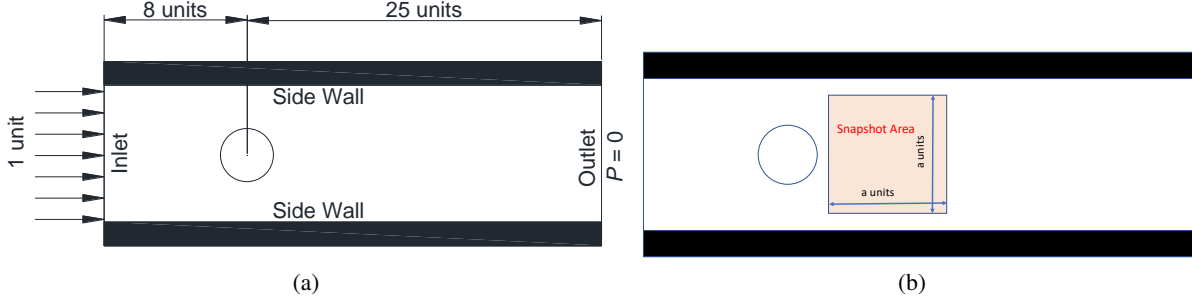


Figure 5: (a) Schematic representation of the computational domain with boundary conditions at the inlet and the outlet. The cylinder has a diameter of 1 unit. A no-slip boundary is considered at the cylinder wall. Zero pressure gradient at the inlet and zero velocity gradient at the outlet are considered. (b) Schematic of the problem domain with snapshot cutout of $a \times a$. For flow past cylinder problems, $a = 4$ units. *The schematics are not to scale.*

Fig. 3 shows the prediction of Enseners for x and y velocity components at various times in simulation with 16 sensors. We see that it produces results that accurately captures the current state of the system at most points in the domain. If a network is trained without a physics-based loss function then it will produce garbage values at points where data is absent. Fig 4 shows violin plot of error vector ϵ defined in Eq. (19) between target and prediction with various noise level in sensor measurement for test case. In Eq. (19), m for x velocity and y velocity are 0 and 1 respectively and $\gamma^* = 2$. The plot represents the distribution of error ϵ in the prediction vector. Greater spread corresponding to a point on the y -axis corresponds to more values present in the error vector ϵ around that value of the point on the y -axis. We see the model is robust to noise as the mean error in the plot are close for cases of no noise ($SNR_{dB} = None$) and high noise ($SNR_{dB} = 10$).

3.3 Experiment: Flow Past Cylinder

As the second example, we consider the flow past a cylinder problem. It is a well known canonical problem and is characterized by periodic laminar flow vortex shedding. System is governed by incompressible, laminar, Newtonian fluid equations:

$$\frac{\partial(u)}{\partial x} + \frac{\partial(v)}{\partial y} = 0 \quad (26a)$$

$$\frac{\partial(u)}{\partial t} + u \frac{\partial(u)}{\partial x} + v \frac{\partial(u)}{\partial y} = -\frac{1}{\rho} \frac{\partial(p)}{\partial x} + \nu \left(\frac{\partial^2(u)}{\partial x^2} + \frac{\partial^2(u)}{\partial y^2} \right) \quad (26b)$$

$$\frac{\partial(v)}{\partial t} + u \frac{\partial(v)}{\partial x} + v \frac{\partial(v)}{\partial y} = -\frac{1}{\rho} \frac{\partial(p)}{\partial y} + \nu \left(\frac{\partial^2(v)}{\partial x^2} + \frac{\partial^2(v)}{\partial y^2} \right) \quad (26c)$$

3.3.1 Data-set and Model Parameters

A schematic representation of the computational domain is shown in Fig. 5(a). The circular cylinder is considered to have a diameter of 1 unit. The center of the cylinder is located at a distance of 8 units from the inlet. The outlet is located at a distance of 25 units from the center of the cylinder. The sidewalls are at 4 units distance from the center of the cylinder. At the inlet boundary, a uniform velocity of 1 unit along the X -direction is applied. Pressure boundary condition with $P = 0$ is considered at the outlet. A no-slip boundary at the cylinder surface is considered. Coordinate of the snapshot cutout stretches from $[1.5, -2] \times [5.5, 2]$ which is discretized into 64×64 points in x and y directions (see Fig. 5(b)).

Table 5: Data-set parameters for Flow Past Cylinder problem.

γ	M	L	z	ω	ν	Re	domain
5	3	25	1	4096	0.005	200	64×64

The data-set is generated by using Unsteady Reynolds-averaged Navier Stokes (URANS) simulation in OpenFoam [47]. The overall problem domain is discretized into 63420 elements with finer mesh near the cylinder. Time step $\delta t = 0.02$

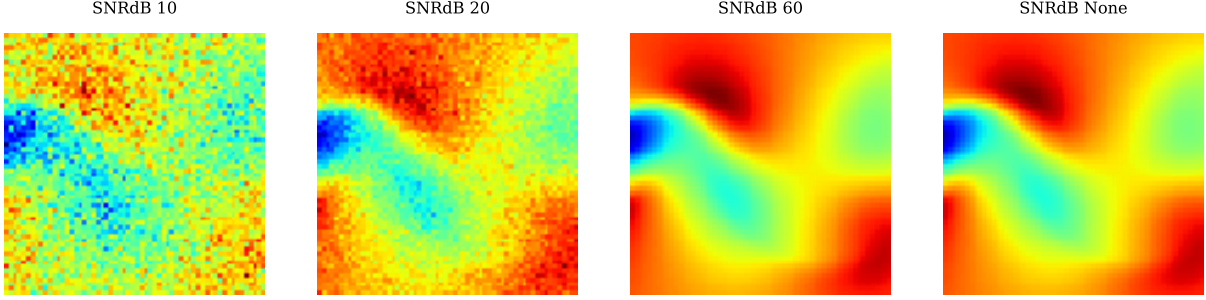


Figure 6: Plots of velocity of Flow Past Cylinder for visualizing different noise levels. SNRdB represents signal to noise ratio in decibels.

units is considered. Code for OpenFOAM simulation can be found at [48]. Parameters related to the data-set considered are displayed in Table 5.

We use a shallow network in the model with two fully connected(FC) layers. Network architecture is displayed in Table 6. We use 500 data nodes for training from each system variable data which is 12.2% of high-resolution data. Training and testing hyper-parameters are shown in table 7 and 8 respectively. Sensor locations for testing are different from the ones used during training. For this problem physics-based loss function is extended to include the continuity equation:

$$P(\chi^k) = \sum_{i=1}^{q+1} \|\text{vec}(W_i - V^n)\|_2^2 + \sum_{i=0}^{\gamma-1} \|\text{vec}\left(\frac{\partial(V_0^n)}{\partial x} + \frac{\partial(V_1^n)}{\partial y}\right)\|_2^2 \quad (27)$$

Table 6: Network architecture of proposed Enzers for Flow Past Cylinder problem.

Layer	Input	Output	Activation
FC	8	64	Softplus
FC	64	$\omega * M * \gamma$	linear

Table 7: Training hyper parameters of Enzers for Flow Past Cylinder.

η_o	η_{i0}	$\hat{\eta}_i$	β	I_o	I_i	ζ_0	$\hat{\zeta}$	p	h	N	ζ
0.0003	0.1	0.002	9	3001	5	0.01	0.0006	16	500	18	8

Table 8: Testing hyper parameters of Enzers for Flow Past Cylinder problem. η_i : inner learning rate, I_i : inner iterations

η_i	I_i	p	\hat{N}
5	100	[4, 16]	12

3.3.2 Results and Discussions

Fig. 7 shows prediction of Enzers for pressure, x and y velocity components with 16 sensors. We see that it produces results that accurately capture the current state of the system at most points in the domain. Fig. 8 shows violin plot of error defined in Eq. (19) between target and prediction with various noise levels in sensor measurement for the test case. In Eq. (19), m for x velocity, y velocity and pressure are 0, 1 and 2 respectively and $\gamma^* = 2$. The plot represents the distribution of error in prediction vectors. We see model is robust to noise as mean error in Fig 8 are close for cases of no noise($SNR_{dB} = None$) and high noise($SNR_{dB} = 10$).

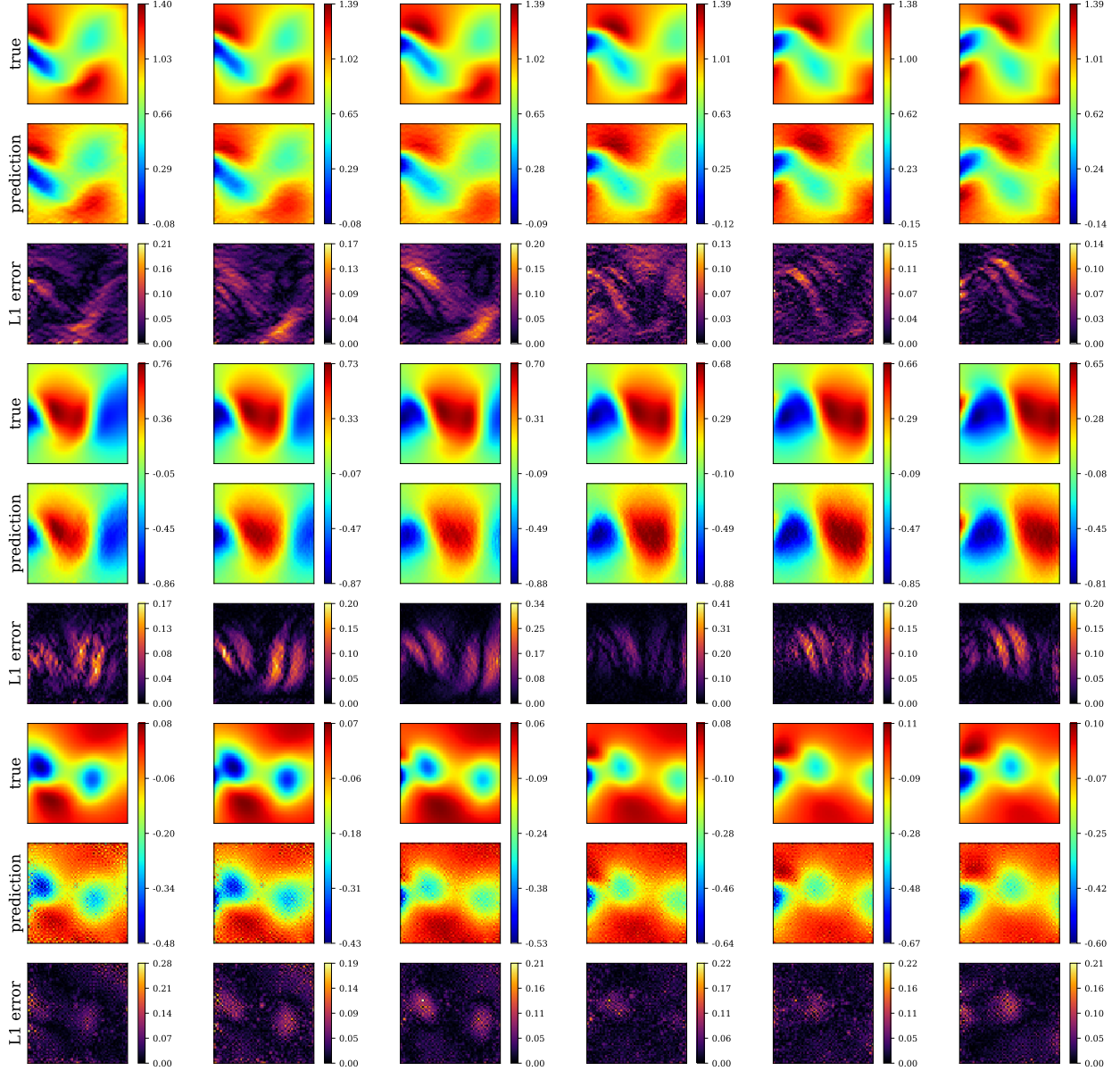


Figure 7: Enser's predictions of a Flow Past Cylinder test case. (Top to bottom) x-velocity target solution, x-velocity Enser's prediction, x-velocity L1error, y-velocity target solution, y-velocity Enser's prediction, y-velocity L1error, pressure target solution, pressure Enser's prediction and pressure L1error.

4 Continuous space models

4.1 Proposed approach

In this section, we propose a novel deep learning-based continuous framework for state estimation. Prediction of γ high dimensional states is done via multiple passes from a feed-forward neural network (FNN) Γ for every collocation point with coordinate vector X_r using optimized reduced state vectors $\xi^k \in \mathbb{R}^\zeta$:

$$\Gamma(\Xi_r^k) = \{D_{mr}^{ki} \in \mathbb{R} \mid i = 0, \dots, \gamma - 1, m = 0, \dots, M - 1\}, \quad r = 0, \dots, \omega \quad (28)$$

$$\Xi_r^k = \{\xi^k, X_r\}, \quad r = 0, \dots, \omega \quad (29)$$

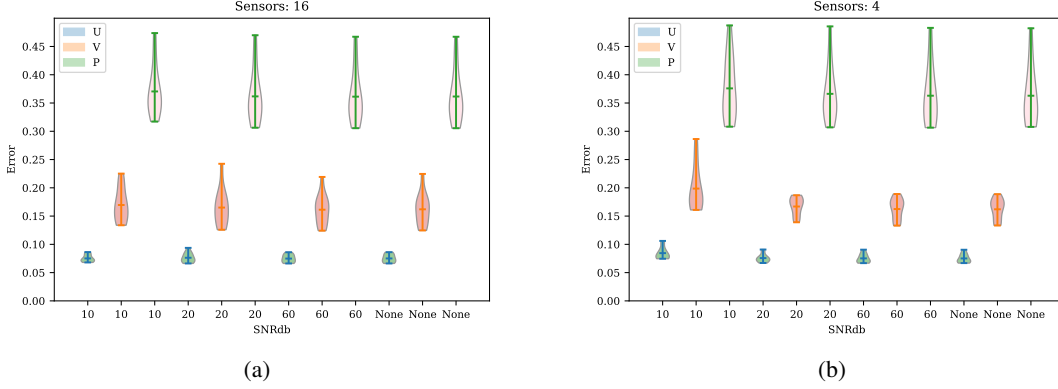


Figure 8: Violin plot representing error ε distribution in prediction vector of x,y velocity and pressure for different noise levels in sensor measurements for Flow Past Cylinder test case.

where output vector of FNN Γ has dimension $\gamma * M$, D_{mr}^{ki} is predicted states value at r^{th} collocation point, X_r are coordinates of r^{th} collocation point. Output of ω FNNs are combined to form third-order tensor $D^k \in \mathbb{R}^{\gamma \times M \times \omega}$. Reduced state is obtained by solving the following minimization problem using sensor data χ^k and predicted states by the neural network.

$$\xi^k = \arg \min_{\xi^k} \|\text{vec}(\chi^k - \rho(\tilde{\Xi}^k))\|_2^2 \quad (30a)$$

$$\rho(\tilde{\Xi}^k) = \{\tilde{Q}_m^{ki} \in \mathbb{R}^p \mid i = 0, \dots, \gamma - 1, m = 0, \dots, M - 1\} \quad (30b)$$

$$\tilde{Q}_m^{ki} = \Lambda_m^{kz+i} \tilde{D}_m^{ki} \quad (30c)$$

$$\Gamma(\tilde{\Xi}_r^k) = \{\tilde{D}_{mr}^{ki} \in \mathbb{R} \mid i = 0, \dots, \gamma - 1, m = 0, \dots, M - 1\}, \quad r = 0, \dots, \omega \quad (30d)$$

$$\tilde{\Xi}_r^k = \{\tilde{\xi}^k, X_r\}, \quad r = 0, \dots, \omega \quad (30e)$$

where $\tilde{Q}_m^{ki} \in \mathbb{R}^p$ are values of predicted states at sensor locations λ_m^{kz+i} . Note that in practice ξ^k is obtained by a few steps of gradient descent instead of global minimization. The network is trained by minimizing data loss and physics-based loss $P(\chi^k)$ across training samples N .

$$\theta^* = \arg \min_{\theta} \sum_{k=0}^{N-1} \|\text{vec}(\phi^k - \Upsilon(\chi^k))\|_2^2 + P(\chi^k) \quad (31a)$$

$$\Upsilon(\chi^k) = \{Y_m^{ki} \in \mathbb{R}^h \mid i = 0, \dots, \gamma - 1, m = 0, \dots, M - 1\} \quad (31b)$$

$$Y_m^{ki} = \Pi_m^{kz+i} D_m^{ki} \quad (31c)$$

where $D_m^{ki} \in \mathbb{R}^\omega$ are predicted states from Eq. (28), $Y_m^{ki} \in \mathbb{R}^h$ are values of predicted states at data locations π_m^{kz+i} , $\Upsilon(\chi^k) \in \mathbb{R}^{\gamma \times M \times p}$ are predicted states composed of γ time steps, θ are network parameters. Fig. 1 shows the network architecture during training. Equations (28) and (30) together forms the implicit optimization layer shown in the Fig. 1 for the continuous model. Training and testing procedure is shown in Algorithm 3 and 4 respectively.

Algorithm 3: Training ENSERS

```

1: Inputs:  $Z, S, T$ . {Eq. (2), Eq. (3), Eq. (4)}
2: Set Hyper-parameters:  $\eta_o$ : outer learning rate,  $\eta_{i0}$ : inner learning rate at epoch=0,  $\hat{\eta}_i$ : inner learning rate rate,  $\beta$ :
   batch size,  $I_o$ : outer iterations,  $I_i$ : inner iterations,  $\hat{\zeta}$ : physics penalty rate,  $\zeta_0$ : physics penalty at epoch=0,  $N$ :
   number of train samples,  $z, \gamma$ .
3: Calculate data-set:  $\chi, \phi, \Lambda, \Pi$ 
4: Initialize: Neural network model:  $\Gamma(\cdot; \theta)$ 
5: for  $\iota_o = 0$  to  $I_o - 1$  do {Outer optimization Loop}
6:    $\eta_i = \eta_{i0} + \iota_o \hat{\eta}_i$  {Schedule inner learning rate}
7:    $\zeta = \zeta_0 + \iota_o \hat{\zeta}$  {Schedule physics penalty}
8:   for  $k = 0$  to  $N - 1$  do
9:     Initialize:  $\tilde{\xi}^k$ 
10:    for  $\iota_i = 0$  to  $I_i - 1$  do {Inner optimization Loop}
11:       $\tilde{\Xi}_r^k = \{\tilde{\xi}^k, X_r\}, \quad r = 0, \dots, \omega$ 
12:       $\tilde{D}_r^k = \Gamma(\tilde{\Xi}_r^k), \quad r = 0, \dots, \omega$  {Eq. (30d)}
13:       $\tilde{Q}^k \leftarrow \text{DrawValuesAtSensorLocations}(\tilde{D}^k)$  {Eq. (30c)}
14:       $\mathcal{L} = \text{MSE}(\chi^k, \tilde{Q}^k)$ 
15:       $\frac{\partial \mathcal{L}}{\partial \tilde{\xi}^k} \leftarrow \text{Backprop}(\mathcal{L})$ 
16:       $\tilde{\xi}^k = \tilde{\xi}^k - \eta_i \frac{\partial \mathcal{L}}{\partial \tilde{\xi}^k}$ 
17:    end for
18:     $\hat{X}_r = X_r$ 
19:     $\Xi_r^k = \{\tilde{\xi}^k, \hat{X}_r\}, \quad r = 0, \dots, \omega$ 
20:     $D_r^k = \Gamma(\Xi_r^k), \quad r = 0, \dots, \omega$  {Eq. (28)}
21:     $Y^k \leftarrow \text{DrawValuesAtDataLocations}(D^k)$  {Eq. (31c)}
22:     $\mathcal{L} = \text{MSE}(\phi^k, Y^k) + \zeta P(D^k)$  {Calculate loss}
23:     $\frac{\partial \mathcal{L}}{\partial \theta} \leftarrow \text{Backprop}(\mathcal{L})$ 
24:     $\theta \leftarrow \theta - \eta_o \frac{\partial \mathcal{L}}{\partial \theta}$  {Update weights}
25:  end for
26: end for
27: Output: Trained network  $\Gamma(\cdot; \theta^*)$ .

```

4.1.1 Physics-based loss function

The physics-based loss function for continuous space models differs from discrete formulation due to how RHS of Eq. (1) i.e. F is evaluated. In this case, we use automatic differentiation for calculating gradients w.r.t. coordinates used in F . For example in first case of Allen–Cahn equation \hat{F} is evaluated as:

$$\hat{F}_r = 0.0001 \frac{\partial^2 u}{\partial \hat{X}_r^2} + 5u^3 - 5u, \quad r = 0, \dots, \omega \quad (32)$$

where \hat{X}_r is coordinate vector concatenated with optimized reduced state vector at end of inner optimization loop, see line 18 in algorithm (3). In second case of Convection-diffusion equation \hat{F} is evaluated as:

$$\hat{F}_r = a(x, y) \frac{\partial u}{\partial \hat{X}_r^0} + b(x, y) \frac{\partial u}{\partial \hat{X}_r^1} + c \frac{\partial^2 u}{\partial \hat{X}_r^{0^2}} + d \frac{\partial^2 u}{\partial \hat{X}_r^{1^2}}, \quad r = 0, \dots, \omega. \quad (33)$$

where \hat{X}_r^0, \hat{X}_r^1 are x and y coordinate respectively, a, b, c, d are defined in Eq. 36.

Algorithm 4: Testing ENSERS

- 1: **Inputs:** Trained network $\Gamma(\cdot; \theta^*)$, S . {Eq. (3)}
 - 2: **Set Hyper-parameters:** η_i : inner learning rate, I_i : inner iterations, \hat{N} : number of test samples, z , γ .
 - 3: **Calculate data-set:** \mathcal{X} , Λ
 - 4: **for** $k = 0$ to $\hat{N} - 1$ **do**
 - 5: **Initialize:** $\tilde{\xi}^k$
 - 6: **for** $i_i = 0$ to $I_i - 1$ **do** {Inner optimization Loop}
 - 7: $\tilde{\Xi}_r^k = \{\tilde{\xi}^k, X_r\}$, $r = 0, \dots, \omega$
 - 8: $\tilde{D}_r^k = \Gamma(\tilde{\Xi}_r^k)$, $r = 0, \dots, \omega$ {Eq. (30d)}
 - 9: $\tilde{Q}^k \leftarrow \text{DrawValuesAtSensorLocations}(\tilde{D}^k)$ {Eq. (30c)}
 - 10: $\mathcal{L} = \text{MSE}(\mathcal{X}^k, \tilde{Q}^k)$
 - 11: $\frac{\partial \mathcal{L}}{\partial \tilde{\xi}^k} \leftarrow \text{Backprop}(\mathcal{L})$
 - 12: $\tilde{\xi}^k = \tilde{\xi}^k - \eta_i \frac{\partial \mathcal{L}}{\partial \tilde{\xi}^k}$
 - 13: **end for**
 - 14: $\Xi_r^k = \{\tilde{\xi}^k, X_r\}$, $r = 0, \dots, \omega$
 - 15: $D_r^k = \Gamma(\Xi_r^k)$, $r = 0, \dots, \omega$ {Eq. (28)}
 - 16: **end for**
 - 17: **Output:** Predicted states $\{D_m^{ki} \mid k = 0, \dots, N - 1, i = 0, \dots, \gamma - 1, m = 0, \dots, M - 1\}$.
-

4.2 Experiment: Allen–Cahn equation

We consider the Allen–Cahn equation along with periodic boundary conditions. The Allen–Cahn equation is a well-known equation from the area of reaction-diffusion systems. It describes the process of phase separation in multicomponent alloy systems, including order-disorder transitions.

$$\begin{aligned}
u_t - 0.0001u_{xx} + 5u^3 - 5u &= 0, & x \in [-1, 1], t \in [0, 1], \\
u(0, x) &= x^2 \cos(\pi x), \\
u(t, -1) &= u(t, 1), \\
u_x(t, -1) &= u_x(t, 1).
\end{aligned} \tag{34}$$

4.2.1 Data-set and Model Parameters

Data-set is generated by simulating the Allen–Cahn equation (34) using conventional spectral methods. Starting from an initial condition $u(0, x) = x^2 \cos(\pi x)$ and assuming periodic boundary conditions $u(t, -1) = u(t, 1)$ and $u_x(t, -1) = u_x(t, 1)$, we integrated Eq. (34) up to a final time $t = 1.0$ using the Chebfun package [49] with a spectral Fourier discretization with 512 modes and a fourth-order explicit Runge–Kutta temporal integrator with time-step $\Delta t = 10^{-5}$. For more details on the data-set see [41]. Plots depicting different noise levels used for sensor measurement during testing are shown in Fig. 9.

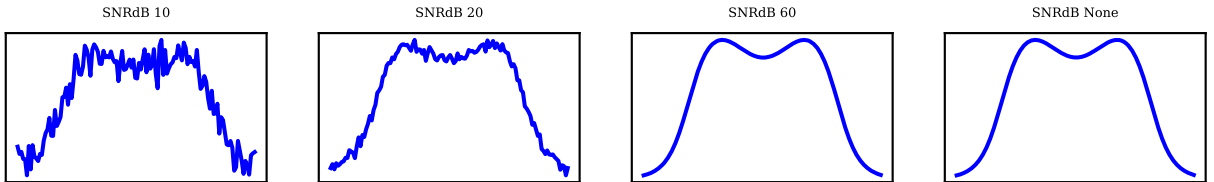


Figure 9: Data plots of Allen–Cahn equation for visualizing different noise levels. SNRdB represents signal to noise ratio in decibels.

The network considered in the continuous formulation has significantly fewer weights compared to the discrete one. This is because the output of the network is predicted at a single point. Network architecture is shown in table 10. The input size of the network is equal to the sum of the size of the reduced state ζ and the dimension of coordinates. For training we use 10 data nodes p which is 7.81% of 128 total nodes ω . Similar to previous cases inner loop learning rate

Table 9: Data-set parameters for Allen–Cahn equation.

γ	M	L	z	ω	domain
5	1	50	1	128	128

η_i and physics loss penalty ζ are increased linearly with each epoch. Other training and testing hyperparameters are shown in table 11 and 12 respectively.

Table 10: Network architecture of proposed Enzers for Allen–Cahn equation.

Layer	Input	Output	Activation
FC	7	128	Tanh
FC	128	128	Tanh
FC	128	128	Tanh
FC	128	128	Tanh
FC	128	$M * \gamma$	linear

Table 11: Training hyper parameters of Enzers for Allen–Cahn equation.

η_o	η_{i0}	$\hat{\eta}_i$	β	I_o	I_i	ζ_0	$\hat{\zeta}$	p	h	N	ζ
0.001	0.005	$6e-5$	10	1201	8	0.01	$2e-5$	10	10	40	6

Table 12: Testing hyper parameters of Enzers for Allen–Cahn equation. η_i : inner learning rate, I_i : inner iterations

η_i	I_i	p	\hat{N}
0.1	50	[6, 16]	12

4.2.2 Results and Discussions

Fig. 10 shows the prediction of Enzers with 16 sensors. A noticeable benefit of the continuous formulation is that prediction is smooth compared to discrete cases. Fig. 11 shows violin plot of L2 error defined in Eq. (19) between target and prediction with various noise levels in sensor measurement for the test case. In Eq. (19), $m = 0$ and $\gamma^* = 2$. Similar to discrete cases, the model is robust to noise in measurements. Fig. 11 shows a marginal increase in error with noise in the case of 16 sensors. Also, error bars with 6 sensors are similar to 16 sensors with low noise and increase slowly with noise.

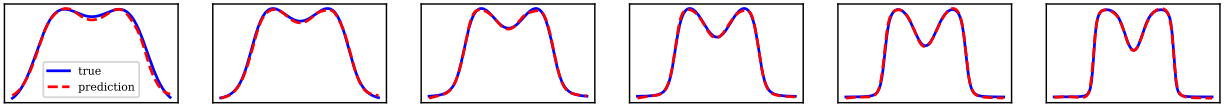


Figure 10: Enzers predictions of a Allen–Cahn equation test case with 16 sensors and no noise.

4.3 Experiment: Convection-diffusion equations

Next we consider a 2-dimensional linear variable-coefficient convection-diffusion equation on $\omega = [0, 2\pi] \times [0, 2\pi]$,

$$u_t = a(x, y)u_x + b(x, y)u_y + cu_{xx} + du_{yy} \quad (t, x, y) \in [0, 0.2] \times \omega \quad (35)$$

$$\begin{aligned} a(x, y) &= 0.5(\cos(y) + x(2\pi - x)\sin(x)) + 0.6 \\ b(x, y) &= 2(\cos(y) + \sin(x)) + 0.8 \\ c &= 0.2, d = 0.3 \end{aligned} \quad (36)$$

Convection-diffusion equations are classical PDEs that are used to describe physical phenomena where particles, energy, or other physical quantities are transferred inside a physical system due to two processes namely diffusion

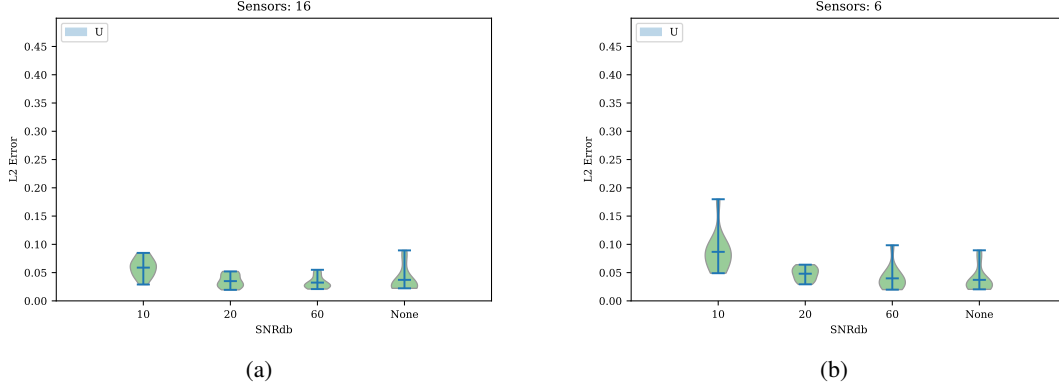


Figure 11: Violin plot representing error ϵ distribution in prediction vector of data, for different noise levels in sensor measurements for Allen–Cahn equation test case.

and convection. These equations are widely applied in many scientific areas and industrial fields, such as pollutants dispersion in rivers or atmosphere, solute transferring in a porous medium, and oil reservoir simulation. We consider variables convection and diffusion coefficients Eq. (36) in this experiment.

4.3.1 Data-set and Model Parameters

Data is generated by solving the problem (35) using a high precision numerical scheme with a pseudo-spectral method for spatial discretization and 4th order Runge-Kutta for temporal discretization (with time step size $\delta t = 0.01$). We assume periodic boundary conditions and the initial value

$$u(x, y, 0) = \sum_{|k|, |l| \leq N} \lambda_{k,l} \cos(kx + ly) + \gamma_{k,l} \sin(kx + ly) \tag{37}$$

where $N = 9$, $\lambda_{k,l}, \gamma_{k,l} \sim \mathcal{N}(0, 0.02)$, and k and l are chosen randomly. For more details on the data-set see [50]. Noisy data used for sensor measurement during testing is shown in Fig. 12 with various noise levels at a particular time. We use a simulation of length 40 as shown in table 13 along with other data parameters.

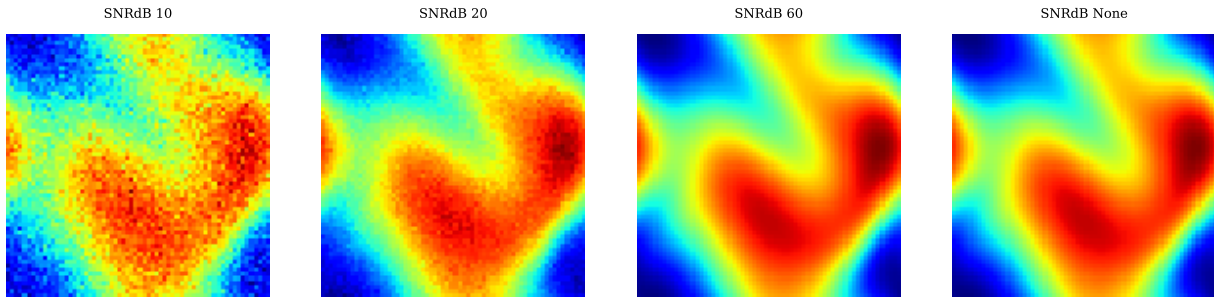


Figure 12: Data plots of Convection-diffusion equation for visualizing different noise levels. SNRdB represents signal to noise ratio in decibels.

Table 13: Data-set parameters for Convection-diffusion equation.

γ	M	L	z	ω	domain
5	1	40	1	4096	64×64

Network architecture is shown in table 14. Similar to the previous case a deep network with 5 layers and a small output size is used. The activation function is Tanh, which also has a continuous first derivative. For training, we use $p = 1024$

Table 14: Network architecture of proposed Enzers for Convection-diffusion equation.

Layer	Input	Output	Activation
FC	8	128	Tanh
FC	128	256	Tanh
FC	256	256	Tanh
FC	256	128	Tanh
FC	128	$M * \gamma$	linear

Table 15: Training hyper parameters of Enzers for Convection-diffusion equation.

η_o	η_{i0}	$\hat{\eta}_i$	β	I_o	I_i	ζ_0	$\hat{\zeta}$	p	h	N	ζ
0.0005	0.005	$5e-5$	11	1001	10	0.005	$1e-5$	32	1024	33	6

Table 16: Testing hyper parameters of Enzers for Convection-diffusion equation. η_i : inner learning rate, I_i : inner iterations

η_i	I_i	p	\hat{N}
0.2	50	[4, 16]	12

training nodes i.e. 25% of total nodes. Training and testing hyperparameters are shown in tables k and ll respectively. Inner loop learning rate η_i and physics loss penalty ζ are increased linearly with each epoch.

4.3.2 Results and Discussions

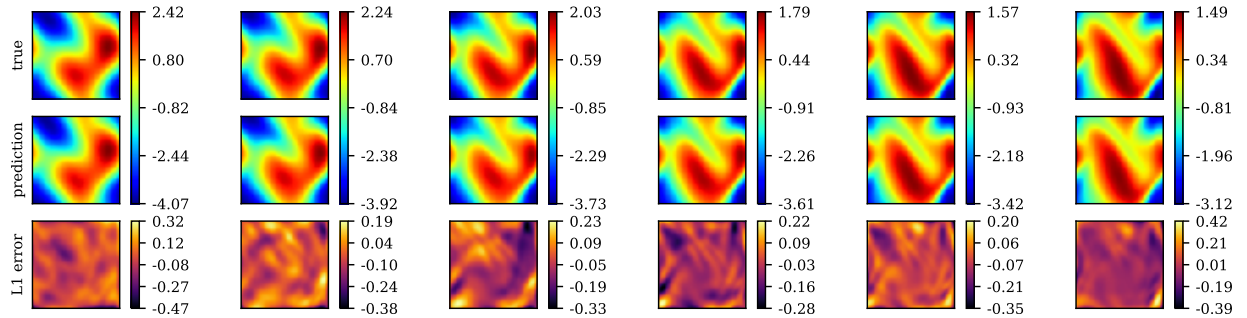


Figure 13: Enzers predictions of a Convection-diffusion equation test case. (Top to bottom) Target solution, Enzers prediction, L1error.

Fig. 13 shows the prediction of the Enzers with 16 sensors. The model is able to predict the state accurately and with little distortion. Fig. 14 shows violin plot of L2 error defined in Eq. (19) between target and prediction with various noise levels in sensor measurement for the test case. In Eq. (19), $m = 0$ and $\gamma^* = 2$ i.e. we use middle prediction out γ time steps. We see the model is robust to noise as the mean error in the plots are close for cases of no noise($SNR_{dB} = None$) and high noise($SNR_{dB} = 10$) for 16 sensors case and increases slightly noise for 4 sensor cases. Training continuous model for two dimensions takes more time than discrete because of the increased number of collocation points and multiple automatic differentiation required for calculating loss function.

5 Conclusions

In this work, we develop a novel technique to learn a deep learning model from sparse moving training labels for which model reduction is nontrivial. The method uses an implicit optimization layer for minimizing the energy of the solution implemented through the technique of unrolled differentiation. We proposed two formulations based on this technique for discrete and continuous prediction in space. For learning from sparse training labels we included a physics-based loss function calculated via convolutional filters in the discrete formulation and via automatic differentiation in the continuous formulation. Where most deep learning-based methods assume fixed sensors Enzers is capable of predicting full states given a varied number of sensors at random locations.

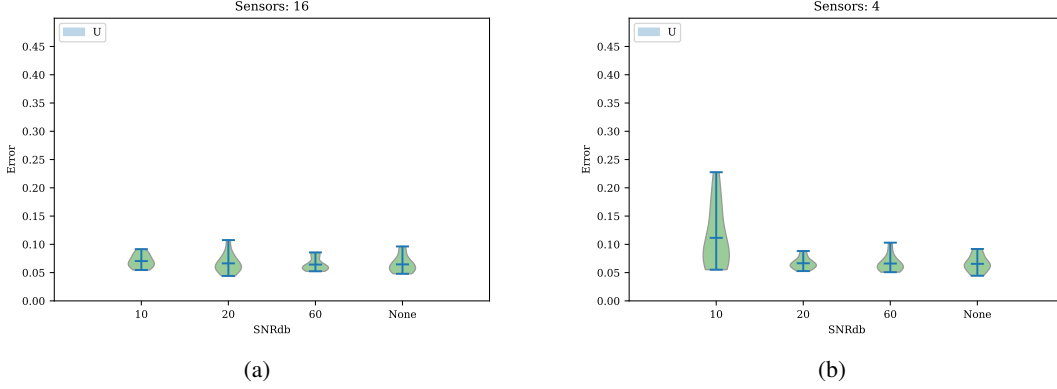


Figure 14: Violin plot representing error ε distribution in prediction vector of x,y velocity and pressure for different noise levels in sensor measurements for Convection-diffusion equation test case.

We demonstrate the model performance using two-fluid problems of 2D coupled Burgers' equation and Flow Past Cylinder for the discrete case. For the continuous case, we used two problems namely Allen–Cahn equation and the Convection-diffusion equation. Model is shown to be robust against noisy sensor measurements. Future work can be aimed at quantifying uncertainty in such networks. Another direction can be to train networks for future states only using initial and boundary conditions.

Acknowledgements

SC acknowledges the financial support received from Science and Engineering Research Board (SERB) via project no. SRG/2021/000467 and Indian Institute Of Technology–Delhi in form of seed grant.

Reproducibility

The codes associated with the paper will be released on acceptance.

A Convolution operators for gradient and laplacian terms

Sobel Filter used to estimate 1st-order gradient is:

$$E = \begin{bmatrix} 1 & -8 & 0 & 8 & -1 \\ 2 & -16 & 0 & 16 & -2 \\ 3 & -24 & 0 & 24 & -3 \\ 2 & -16 & 0 & 16 & -2 \\ 1 & -8 & 0 & 8 & -1 \end{bmatrix} \quad (38a)$$

$$\frac{\partial}{\partial x} = E \times \frac{1}{9 * 12 \delta x} \quad (38b)$$

Filter used to estimate laplacian is:

$$\frac{\partial}{\partial y} = E^T \times \frac{1}{9 * 12 \delta y} \quad (38c)$$

$$\frac{\partial^2}{\partial x^2} + \frac{\partial^2}{\partial y^2} filter = \begin{bmatrix} 0 & 0 & -1 & 0 & 0 \\ 0 & 0 & 16 & 0 & 0 \\ -1 & 16 & -60 & 16 & -1 \\ 0 & 0 & 16 & 0 & 0 \\ 0 & 0 & -1 & 0 & 0 \end{bmatrix} \times \frac{1}{12 \delta x \delta y} \quad (39)$$

References

- [1] L. Cordier, Springer Vienna, 2011. doi:10.1007/978-3-7091-0758-4_1.
- [2] R. Semaan, M. Y. El Sayed, R. Radespiel, Springer International Publishing, Cham, 2019.
- [3] S. Sankaran, M. Esmaily Moghadam, A. M. Kahn, E. E. Tseng, J. M. Guccione, A. L. Marsden, Patient-specific multiscale modeling of blood flow for coronary artery bypass graft surgery, *Ann Biomed Eng* 40 (2012) 2228–2242.
- [4] A. Yakhot, T. Anor, G. E. Karniadakis, A reconstruction method for gappy and noisy arterial flow data, *IEEE Trans Med Imaging* 26 (2007) 1681–1697.
- [5] G. Kissas, Y. Yang, E. Hwuang, W. R. Witschey, J. A. Detre, P. Perdikaris, Machine learning in cardiovascular flows modeling: Predicting arterial blood pressure from non-invasive 4d flow mri data using physics-informed neural networks, *Computer Methods in Applied Mechanics and Engineering* 358 (2020) 112623. URL: <https://www.sciencedirect.com/science/article/pii/S0045782519305055>. doi:<https://doi.org/10.1016/j.cma.2019.112623>.
- [6] M. D. Graziano, M. D’Errico, G. Rufino, Ship heading and velocity analysis by wake detection in sar images, *Acta Astronautica* 128 (2016) 72–82. URL: <https://www.sciencedirect.com/science/article/pii/S0094576516300303>. doi:<https://doi.org/10.1016/j.actaastro.2016.07.001>.
- [7] E. Kalnay, *Atmospheric Modeling, Data Assimilation and Predictability*, Cambridge University Press, 2002. doi:10.1017/CB09780511802270.
- [8] F. Ong, M. Uecker, U. Tariq, A. Hsiao, M. T. Alley, S. S. Vasanawala, M. Lustig, Robust 4d flow denoising using divergence-free wavelet transform, *Magnetic Resonance in Medicine* 73 (2015) 828–842. URL: <https://onlinelibrary.wiley.com/doi/abs/10.1002/mrm.25176>. doi:<https://doi.org/10.1002/mrm.25176>. arXiv:<https://onlinelibrary.wiley.com/doi/pdf/10.1002/mrm.25176>.
- [9] F. M. Callaghan, S. M. Grieve, Spatial resolution and velocity field improvement of 4D-flow MRI, *Magn Reson Med* 78 (2017) 1959–1968.
- [10] M. F. Fathi, A. Bakhshinejad, A. Baghaie, D. Saloner, R. H. Sacho, V. L. Rayz, R. M. D’Souza, Denoising and spatial resolution enhancement of 4D flow MRI using proper orthogonal decomposition and lasso regularization, *Comput Med Imaging Graph* 70 (2018) 165–172.
- [11] C. M. Bishop, *Pattern recognition and machine learning*, springer, 2006.
- [12] K. Reif, S. Gunther, E. Yaz, R. Unbehauen, Stochastic stability of the discrete-time extended kalman filter, *IEEE Transactions on Automatic control* 44 (1999) 714–728.
- [13] E. A. Wan, R. Van Der Merwe, S. Haykin, The unscented kalman filter, *Kalman filtering and neural networks* 5 (2001) 221–280.
- [14] J. Tu, J. Griffin, A. Hart, C. Rowley, L. Cattafesta, L. Ukeiley, Integration of non-time-resolved piv and time-resolved velocity point sensors for dynamic estimation of velocity fields, *Experiments in Fluids* 54 (2012). doi:10.1007/s00348-012-1429-7.
- [15] P. Schmid, J. Sesterhenn, Dynamic Mode Decomposition of numerical and experimental data, in: *APS Division of Fluid Dynamics Meeting Abstracts*, volume 61 of *APS Meeting Abstracts*, 2008, p. MR.007.
- [16] C. W. ROWLEY, I. MEZIĆ, S. BAGHERI, P. SCHLATTER, D. S. HENNINGSON, Spectral analysis of nonlinear flows, *Journal of Fluid Mechanics* 641 (2009) 115–127. doi:10.1017/S0022112009992059.
- [17] M. Buffoni, S. Camarri, A. Iollo, E. Lombardi, M. Salvetti, A non-linear observer for unsteady three-dimensional flows, *Journal of Computational Physics* 227 (2008) 2626 – 2643. URL: <http://www.sciencedirect.com/science/article/pii/S0021999107004858>. doi:<https://doi.org/10.1016/j.jcp.2007.11.005>.
- [18] R. Adrian, On the role of conditional averages in turbulence theory., 1975.
- [19] Y. G. Guezennec, Stochastic estimation of coherent structures in turbulent boundary layers, *Physics of Fluids A: Fluid Dynamics* 1 (1989) 1054–1060. URL: <https://doi.org/10.1063/1.857396>. doi:10.1063/1.857396. arXiv:<https://doi.org/10.1063/1.857396>.
- [20] D. Ewing, J. H. Citriniti, Examination of a lse/pod complementary technique using single and multi-time information in the axisymmetric shear layer, in: J. N. Sørensen, E. J. Hopfinger, N. Aubry (Eds.), *IUTAM Symposium on Simulation and Identification of Organized Structures in Flows*, Springer Netherlands, Dordrecht, 1999, pp. 375–384.

- [21] A. M. Naguib, C. E. Wark, O. Juckenhöfel, Stochastic estimation and flow sources associated with surface pressure events in a turbulent boundary layer, *Physics of Fluids* 13 (2001) 2611–2626. URL: <https://doi.org/10.1063/1.1389284>. doi:10.1063/1.1389284. arXiv:<https://doi.org/10.1063/1.1389284>.
- [22] J. P. Bonnet, D. R. Cole, J. Delville, M. N. Glauser, L. S. Ukeiley, Stochastic estimation and proper orthogonal decomposition: Complementary techniques for identifying structure, *Experiments in Fluids* 17 (1994) 307–314. URL: <https://doi.org/10.1007/BF01874409>. doi:10.1007/BF01874409.
- [23] J. Pinier, J. Ausseur, M. Glauser, H. Higuchi, Proportional closed-loop feedback control of flow separation, *Aiaa Journal - AIAA J* 45 (2007) 181–190. doi:10.2514/1.23465.
- [24] R. Adrian, Conditional eddies in isotropic turbulence, *Physics of Fluids* 22 (1979). doi:10.1063/1.862515.
- [25] T. C. Tung, R. J. Adrian, Higher-order estimates of conditional eddies in isotropic turbulence, *The Physics of Fluids* 23 (1980) 1469–1470. URL: <https://aip.scitation.org/doi/abs/10.1063/1.863130>. doi:10.1063/1.863130. arXiv:<https://aip.scitation.org/doi/pdf/10.1063/1.863130>.
- [26] Y. Kumar, P. Bahl, S. Chakraborty, State estimation with limited sensors – a deep learning based approach, 2021. arXiv:2101.11513.
- [27] N. B. Erichson, L. Mathelin, Z. Yao, S. L. Brunton, M. W. Mahoney, J. N. Kutz, Shallow learning for fluid flow reconstruction with limited sensors and limited data, 2019. arXiv:1902.07358.
- [28] N. J. Nair, A. Goza, Leveraging reduced-order models for state estimation using deep learning, *Journal of Fluid Mechanics* 897 (2020) R1. doi:10.1017/jfm.2020.409.
- [29] H. Gao, L. Sun, J.-X. Wang, Super-resolution and denoising of fluid flow using physics-informed convolutional neural networks without high-resolution labels, *Physics of Fluids* 33 (2021) 073603. URL: <https://doi.org/10.1063/5.0054312>. doi:10.1063/5.0054312. arXiv:<https://doi.org/10.1063/5.0054312>.
- [30] E. Grefenstette, B. Amos, D. Yarats, P. M. Htut, A. Molchanov, F. Meier, D. Kiela, K. Cho, S. Chintala, Generalized inner loop meta-learning, arXiv preprint arXiv:1910.01727 (2019).
- [31] B. Amos, Differentiable Optimization-Based Modeling for Machine Learning, Ph.D. thesis, Carnegie Mellon University, 2019.
- [32] I. Goodfellow, M. Mirza, A. Courville, Y. Bengio, Multi-prediction deep boltzmann machines, *Advances in Neural Information Processing Systems* (2013).
- [33] V. Stoyanov, A. Ropson, J. Eisner, Empirical risk minimization of graphical model parameters given approximate inference, decoding, and model structure, in: G. Gordon, D. Dunson, M. Dudík (Eds.), *Proceedings of the Fourteenth International Conference on Artificial Intelligence and Statistics*, volume 15 of *Proceedings of Machine Learning Research*, PMLR, Fort Lauderdale, FL, USA, 2011, pp. 725–733. URL: <https://proceedings.mlr.press/v15/stoyanov11a.html>.
- [34] P. Brakel, D. Stroob, t. B. Schrauwen, Training energy-based models for time-series imputation, *Journal of Machine Learning Research* 14 (2013) 2771–2797. URL: <http://jmlr.org/papers/v14/brakel13a.html>.
- [35] Y. Lecun, S. Chopra, R. Hadsell, A tutorial on energy-based learning, 2006.
- [36] D. Utama, A. N., M. Iqbal, An optimal generic model for multi-parameters and big data optimizing: a laboratory experimental study, *Journal of Physics: Conference Series* 978 (2018) 012045. doi:10.1088/1742-6596/978/1/012045.
- [37] D. Belanger, B. Yang, A. McCallum, End-to-end learning for structured prediction energy networks, 2017. arXiv:1703.05667.
- [38] L. Metz, B. Poole, D. Pfau, J. Sohl-Dickstein, Unrolled generative adversarial networks (2016).
- [39] M. J. Johnson, D. K. Duvenaud, A. Wiltchko, R. P. Adams, S. R. Datta, Composing graphical models with neural networks for structured representations and fast inference, in: D. Lee, M. Sugiyama, U. Luxburg, I. Guyon, R. Garnett (Eds.), *Advances in Neural Information Processing Systems*, volume 29, Curran Associates, Inc., 2016. URL: <https://proceedings.neurips.cc/paper/2016/file/7d6044e95a16761171b130dcb476a43e-Paper.pdf>.
- [40] C. Jordan-Squire, Convex optimization over probability measures, 2015.
- [41] M. Raissi, P. Perdikaris, G. Karniadakis, Physics-informed neural networks: A deep learning framework for solving forward and inverse problems involving nonlinear partial differential equations, *Journal of Computational Physics* 378 (2019) 686–707. doi:<https://doi.org/10.1016/j.jcp.2018.10.045>.

- [42] Y. Zhu, N. Zabaras, P.-S. Koutsourelakis, P. Perdikaris, Physics-constrained deep learning for high-dimensional surrogate modeling and uncertainty quantification without labeled data, *Journal of Computational Physics* 394 (2019) 56–81. URL: <https://www.sciencedirect.com/science/article/pii/S0021999119303559>. doi:<https://doi.org/10.1016/j.jcp.2019.05.024>.
- [43] N. Geneva, N. Zabaras, Modeling the dynamics of pde systems with physics-constrained deep auto-regressive networks, *Journal of Computational Physics* 403 (2020) 109056. URL: <https://www.sciencedirect.com/science/article/pii/S0021999119307612>. doi:<https://doi.org/10.1016/j.jcp.2019.109056>.
- [44] I. Sobel, G. Feldman, A 3×3 isotropic gradient operator for image processing, *Pattern Classification and Scene Analysis* (1973) 271–272.
- [45] A. Logg, K.-A. Mardal, G. N. Wells, et al., *Automated Solution of Differential Equations by the Finite Element Method*, Springer, 2012. doi:10.1007/978-3-642-23099-8.
- [46] X. Glorot, A. Bordes, Y. Bengio, Deep sparse rectifier neural networks, in: G. Gordon, D. Dunson, M. Dudík (Eds.), *Proceedings of the Fourteenth International Conference on Artificial Intelligence and Statistics*, volume 15 of *Proceedings of Machine Learning Research*, PMLR, Fort Lauderdale, FL, USA, 2011, pp. 315–323. URL: <https://proceedings.mlr.press/v15/glorot11a.html>.
- [47] H. Jasak, Openfoam: open source cfd in research and industry, *International Journal of Naval Architecture and Ocean Engineering* 1 (2009) 89–94.
- [48] R. S. Nithin Adidela, Y. Sudhakar, Laminar flow over a circular cylinder simulation with openfoam v7, <https://github.com/nithinadidela/circular-cylinder>, ????
- [49] T. A. Driscoll, N. Hale, L. N. Trefethen, *Chebfun guide*, 2014.
- [50] Z. Long, Y. Lu, X. Ma, B. Dong, PDE-net: Learning PDEs from data, in: J. Dy, A. Krause (Eds.), *Proceedings of the 35th International Conference on Machine Learning*, volume 80 of *Proceedings of Machine Learning Research*, PMLR, 2018, pp. 3208–3216. URL: <https://proceedings.mlr.press/v80/long18a.html>.